The Astrophysical Journal, 891:28 (14pp), 2020 March 1 https://doi.org/10.3847/1538-4357/ab7233

On the Chemical and Kinematic Consistency between N-rich Metal-poor Field Stars and Enriched Populations in Globular Clusters

Baitian Tang[1], J. G. Fernández-Trincado[2], Chao Liu[3,4], Jincheng Yu[1], Hongliang Yan[3,4], Qi Gao[3,4], Jianrong Shi[3,4], and Douglas Geisler[5,6,7]

[1] School of Physics and Astronomy, Sun Yat-sen University, Zhuhai 519082, People's Republic of China; tangbt@mail.sysu.edu.cn
[2] Instituto de Astronomía y Ciencias Planetarias, Universidad de Atacama, Copayapu 485, Copiapó, Chile
[3] Key Lab of Optical Astronomy, National Astronomical Observatories, Chinese Academy of Sciences, Beijing 100101, People's Republic of China
[4] School of Astronomy and Space Science, University of Chinese Academy of Sciences, Beijing 100049, People's Republic of China
[5] Departamento de Astronomía, Casilla 160-C, Universidad de Concepción, Concepción, Chile
[6] Instituto de Investigación Multidisciplinario en Ciencia y Tecnología, Universidad de La Serena, Av. Raúl Bitrán S/N, La Serena, Chile
[7] Departamento de Astronomía, Facultad de Ciencias, Universidad de La Serena, Av. Juan Cisternas 1200, La Serena, Chile
Received 2019 November 19; revised 2020 January 29; accepted 2020 January 29; published 2020 March 2

Abstract

Interesting chemically peculiar field stars may reflect their stellar evolution history and their possible origin in a different environment from where they are found now; this is one of the most important research fields in Galactic archeology. To explore this further, we have used the CN–CH bands around 4000 Å to identify N-rich metal-poor field stars in LAMOST DR3. Here we expand our N-rich, metal-poor field star sample to ∼100 stars in LAMOST DR5, where 53 of them are newly found in this work. We investigate light elements of common stars between our sample and APOGEE DR14. While Mg, Al, and Si abundances generally agree with the hypothesis that N-rich metal-poor field stars come from enriched populations in globular clusters, it is still inconclusive for C, N, and O. After integrating the orbits of our N-rich field stars and a control sample of normal metal-poor field stars, we find that N-rich field stars have different orbital parameter distributions compared to the control sample—specifically, apocentric distances, maximum vertical amplitude (Z_{max}), orbital energy, and z-direction angular momentum (L_z). The orbital parameters of N-rich field stars indicate that most of them are inner-halo stars. The kinematics of N-rich field stars support their possible GC origin. The spatial and velocity distributions of our bona fide N-rich field star sample are important observational evidence to constrain simulations of the origin of these interesting objects.

Unified Astronomy Thesaurus concepts: Chemically peculiar stars (226); Chemical abundances (224); Stellar kinematics (1608); Globular star clusters (656); Milky Way stellar halo (1060); CN stars (260); Spectroscopy (1317); Stellar dynamics (1596); Milky Way evolution (1052)

Supporting material: machine-readable tables

1. Introduction

With the release of *Gaia* DR2 (Gaia Collaboration et al. 2018; Katz et al. 2019), the proper motions of billions of stars are now available to the astronomical community. Combining with radial velocities from large spectroscopic surveys, like the Sloan Digital Sky Survey (Eisenstein et al. 2011; Blanton et al. 2017), *Gaia*-ESO survey (Gilmore et al. 2012; Randich et al. 2013), and LAMOST Galactic spectroscopic survey (Deng et al. 2012; Zhao et al. 2012), the wealth of 6D information of billions of stars have challenged and even overthrown many aspects of our understanding of the Milky Way (MW). The discovery of snail shells in the phase-space distribution of MW disk stars (Antoja et al. 2018) has inspired debates about their origin: whether they are generated by the passage of a dwarf galaxy (probably the Sagittarius dwarf galaxy) through the MW disk (Binney & Schönrich 2018) or are the echo of the MW bar buckling (Khoperskov et al. 2019). Meanwhile, major accretion events begin to unveil themselves when the stellar distribution in various energy–momentum spaces (e.g., Myeong et al. 2019) is investigated. These major accretion events injected most of the materials from the progenitor dwarf galaxies into our MW, including globular clusters (GCs). As GCs are one of the oldest objects in our Galaxy, identifying and studying accreted GCs help us trace back the accretion history of our Galaxy. Though details of major accretion events, e.g., the number of accretion events and the GCs associated with each event, are still under debate (e.g., Helmi et al. 2018; Massari et al. 2019; Myeong et al. 2019), it is widely accepted that a substantial number of halo stars and GCs were accreted (e.g., Ostdiek et al. 2019). Along the same line, more and more substructures, e.g., stellar streams, are identified inside the MW (e.g., Malhan et al. 2018; Ibata et al. 2019b). An increasing number of stellar streams are suggested to be related to the debris of (inner-halo) GCs (e.g., Ibata et al. 2019a). Aside from these GC destruction events under the influence of Galactic potential, the dynamical relaxation of GCs (e.g., Weinberg 1994; Vesperini & Heggie 1997) also ejects member stars into the field. It would be of great interest to find such GC-ejected stars in order to estimate the mass loss from GCs to better understand the formation and evolution of our MW. To help achieve this goal, another characteristic of GCs is very helpful.

Most GCs are now found to host multiple populations through photometry and spectroscopy (e.g., Carretta et al. 2010b; Mészáros et al. 2015; Milone et al. 2015; Piotto et al. 2015; Tang et al. 2017, 2018). Chemical abundances from spectroscopic data suggest that GCs have a group of so-called "second generation" (SG) stars with enhanced N and Na (sometimes He and Al), but depleted C and O (sometimes Mg). These kinds of stars presumably are only formed in the dense environments of GCs. Therefore, identifying field stars with an SG-like chemical pattern is a feasible way to find a link between field stars and GC ejection/dissolution. Thanks to

large spectroscopic surveys, the search for these chemically peculiar stars is becoming more efficient. Using high spectral resolution surveys, multiple elements, like C, N, O, Na, Mg, and Al, can be measured, depending on the wavelength range and signal-to-noise ratio. Toward this, the Apache Point Observatory Galactic Evolution Experiment (APOGEE; Majewski et al. 2017) and *Gaia*-ESO survey have led to the discovery of a large group of N-rich field stars (Lind et al. 2015; Fernández-Trincado et al. 2016, 2017, 2019a; Martell et al. 2016; Schiavon et al. 2017). While high-resolution spectra give more elements for a detailed investigation of their chemical history, low-resolution spectra can supposedly extend the search for N-rich field stars toward fainter and more numerous samples (Martell & Grebel 2010; Martell et al. 2011; Koch et al. 2019). Simultaneously observing 4000 stars with fibers makes LAMOST an unprecedented machine in collecting low-resolution stellar spectra. Using the CN–CH band features around 4000 Å, we have identified ∼40 N-rich field stars[8] in LAMOST DR3 (Tang et al. 2019, hereafter Paper I). The derived N abundances of these stars are clearly higher than those of the metal-poor field stars, indicating that (1) our sample is a bona fide sample of N-rich field stars and (2) the classical extra-mixing theory may not work for these stars. Moreover, a substantial fraction of retrograding N-rich field stars suggest that some N-rich field stars may be accreted. In this work, we expand our sample to ∼100 N-rich field stars in LAMOST DR5 (Section 2), making it more robust for drawing statistical conclusions, especially for the GC origin of these field stars. We put forward a detailed analysis of high-resolution chemical abundances and kinematics (Sections 3 and 4) to discuss the origins of these N-rich field stars (Section 5). As the second paper of this series, we will also call this present work Paper II.

2. Sample Selection

We first select metal-poor, red giant branch (RGB) field stars according to the same criteria as described in Paper I, which are

1. $4000 < T_{\rm eff} < 5500$ K
2. $\log g < 3.0$
3. $-1.8 < [{\rm Fe/H}] < -1.0$
4. ${\rm S/N}_u > 5.0$

The stellar parameters are derived by the LAMOST Stellar Parameter pipeline (Wu et al. 2011; Luo et al. 2015), with typical uncertainties of 100 K for $T_{\rm eff}$, 0.25 dex for $\log g$, and 0.1 dex for [Fe/H], respectively.

We first check for duplication in the sample and keep the observation for the highest supernova remnant (SNR) for a given star if there were multiple spectra. Then we remove all the stars that have been selected for the parent sample of Paper I. We also check for GC membership using the membership identification method described in Tang et al. (2017). Four possible members of M3 and M10 are excluded. Note that open cluster membership is unlikely, as all open clusters are more metal-rich than $[{\rm Fe/H}] = -1.0$. Thus, our final parent sample consists of 6592 metal-poor field red giants. The $T_{\rm eff}$ versus $\log g$ plot is shown in Figure 1.

Next, we measure the spectral indices of our sample stars. Here we use the definition of the CN3839, CN4142, and CH4300 indices from Harbeck et al. (2003). When correcting

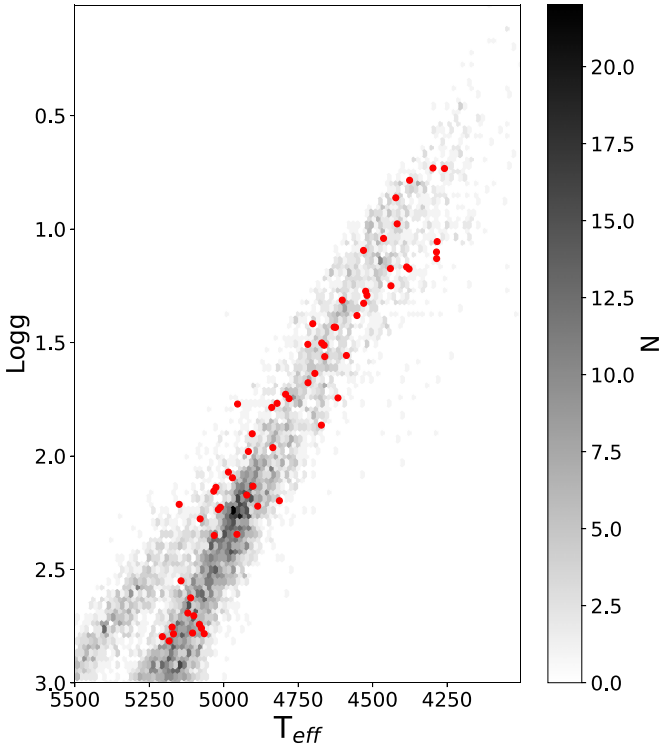

Figure 1. $T_{\rm eff}$ vs. $\log g$ plot. The grayscale map indicates the number density of metal-poor field stars that we selected as the parent sample. The N-rich field stars are shown as red dots.

for radial velocities (RVs) in the LAMOST spectra, we consider the systematic RV shift ($\sim 5\,{\rm km\,s^{-1}}$) reported by Schönrich & Aumer (2017). The selection of N-rich field stars was described in Paper I; here we briefly summarize the selection method. Because CN and CH spectral indices are affected by stellar parameters, especially $T_{\rm eff}$, we plot both CN spectral indices as a function of $T_{\rm eff}$ to first select CN-strong stars that are 2σ above the mean spectral indices of the parent sample stars at the same $T_{\rm eff}$ (Figure 2, green solid lines). Only stars with both strong CN3839 and strong CN4142 are considered as CN-strong stars. Using both CN spectral indices is meant to reduce false positives in the CN-strong star sample. The CN-strong stars are further divided into CH-strong stars and CH-normal stars based on whether their CH spectral indices are above the one σ line (Figure 2 green dashed lines). As we found in Paper I and later show again in this paper, the CN-strong, CH-normal stars are in fact N-rich stars, so we call them N-rich stars in the following text. One improvement that we carry out in this paper is that we subdivide the sample into a more metal-rich sample ($-1.4 < [{\rm Fe/H}] < -1.0$) and a more metal-poor sample ($-1.8 < [{\rm Fe/H}] < -1.4$) in order to further minimize the metallicity effect on spectral indices. We did not attempt to select CN-strong stars based on spectral index versus absolute magnitude plots, because using absolute magnitude may introduce errors from the distance determination (Section 4). The uncertainties of the spectral indices propagated from the typical uncertainties in LAMOST-derived stellar parameters (Luo et al. 2015) are estimated using stellar atmosphere models. The estimated uncertainties of spectral indices are listed in Table 1. The uncertainties are almost negligible compared to the measurements (Table 2).

[8] Also called CN-strong, CH-normal stars in Paper I.

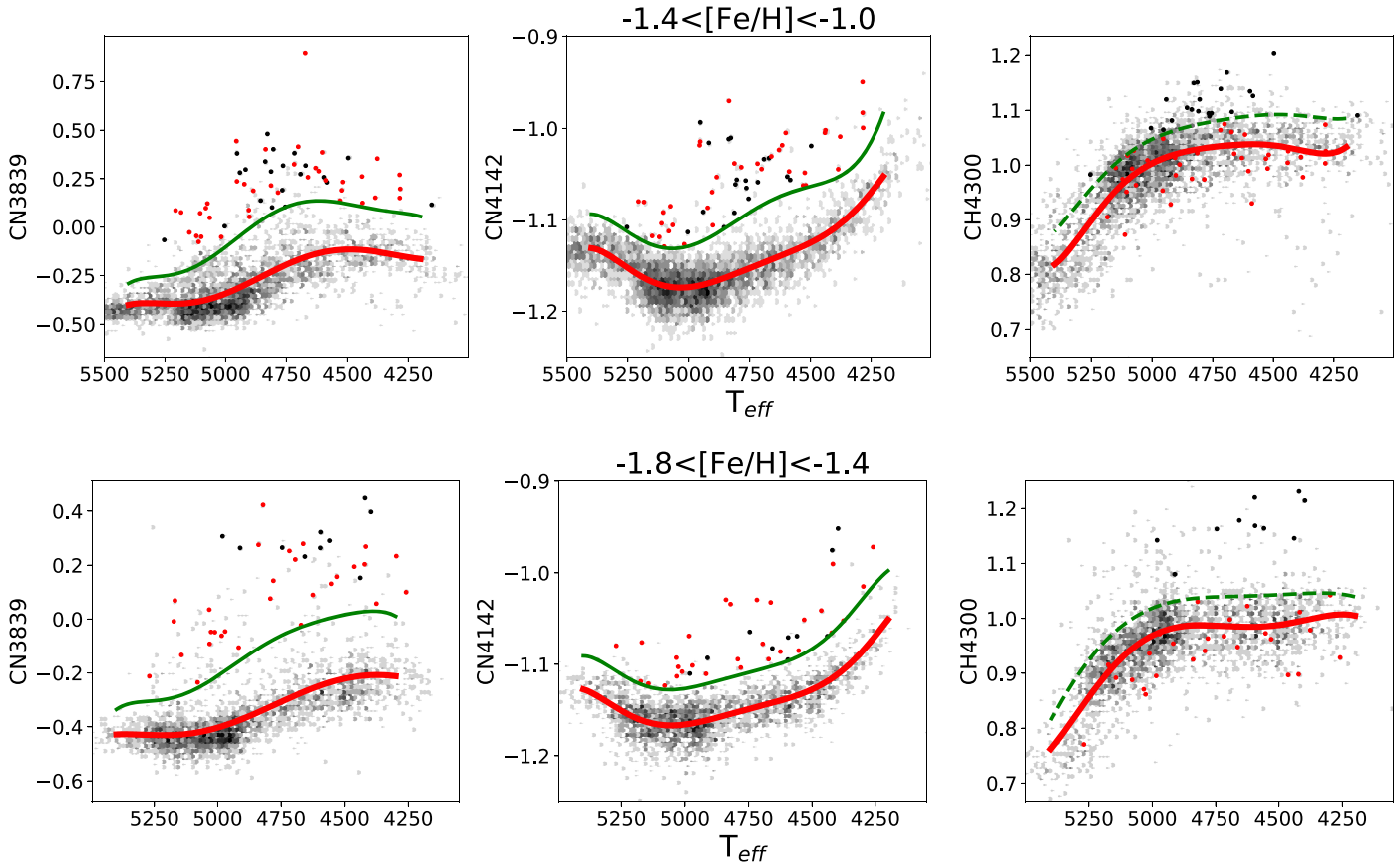

Figure 2. Spectral indices as a function of $T_{\rm eff}$. The grayscale map indicates the number density of metal-poor field stars. The upper panels show the more metal-rich sample ($-1.4 <$ [Fe/H] < -1.0), while the lower panels show the more metal-poor sample ($-1.4 <$ [Fe/H] < -1.8). Red lines are sixth-order polynomials of the mean spectral indices at a step of 100 K. Green solid lines are sixth-order polynomials of the mean spectral indices plus two times standard deviations at a step of 100 K. Similarly, green dashed lines are mean + 1.0 × std. The black dots are CH-strong, CN-strong (C-rich) stars, while the red dots are CH-normal, CN-strong (N-rich) stars. See the text for more details.

Table 1
Uncertainties of Spectral Indices

Index	Metal-rich Sample				Metal-poor Sample			
	$\sigma_{\Delta T\rm eff}$	$\sigma_{\Delta\log g}$	$\sigma_{\Delta\rm [Fe/H]}$	$\sigma_{\rm total}$	$\sigma_{\Delta T\rm eff}$	$\sigma_{\Delta\log g}$	$\sigma_{\Delta\rm [Fe/H]}$	$\sigma_{\rm total}$
CN3839	0.020	0.003	0.015	0.025	0.024	0.000	0.013	0.028
CN4142	0.002	0.003	0.002	0.005	0.007	0.006	0.003	0.009
CH4300	0.013	0.000	0.008	0.015	0.019	0.006	0.008	0.021

Table 2
Spectral Indices of N-rich Field Stars Found in This Paper

#	R.A.	Decl.	CN3839	CN4142	CH4300	δCN3839	δCH4300	Note[a]
1	13.155076	37.698769	0.23	−1.06	1.02	0.35	−0.02	MR
2	245.556824	2.385621	0.19	−1.05	1.00	0.47	−0.02	MR
3	268.058059	26.255920	0.05	−1.11	0.96	0.42	−0.02	MR
..	...	...	...	...	...	...	...	...

Note.
[a] MR denotes the more metal-rich sample, while MP denotes the more metal-poor sample. See text for details.
(This table is available in its entirety in machine-readable form.)

Using this method, we select 67 N-rich stars from the parent sample. After visual examination of these 67 stars, we further exclude two stars with strong nebular emission lines. Thus, we are left with 65 stars as the final sample of this paper (Table 3). As a result, the N-rich field stars constitute about 1% of our parent sample. If only CN3839 is used as the discriminator to separate CN-strong stars from CN-normal stars, the number of CN-strong, CH-normal (N-rich) stars would increase to 160,

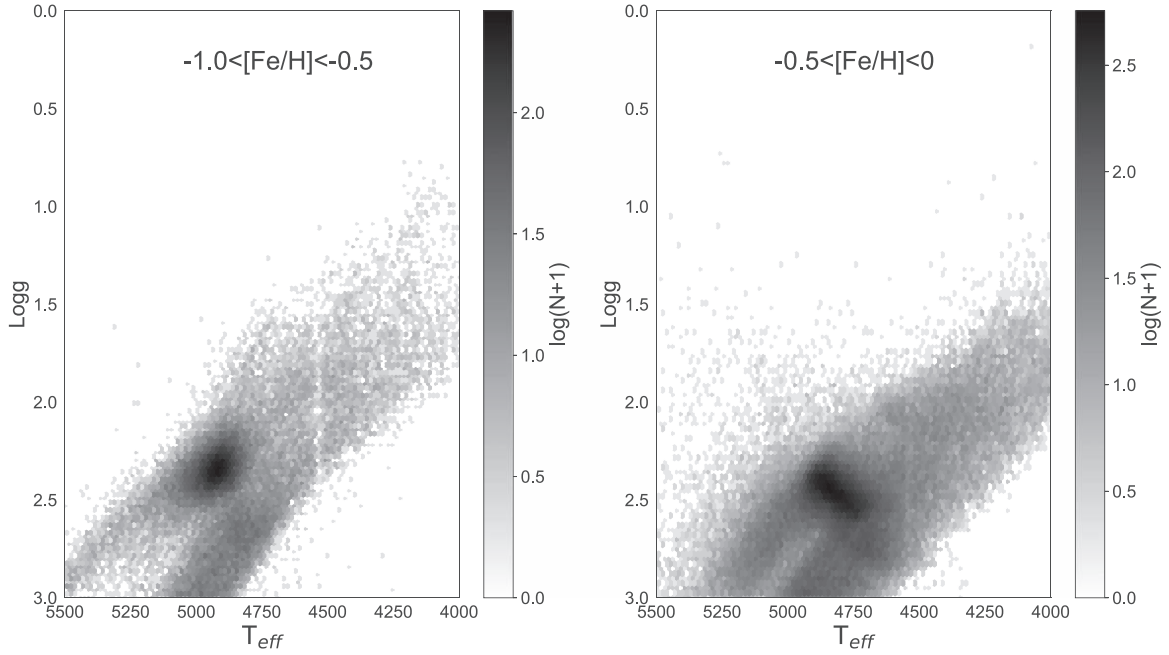

Figure 3. $T_{\rm eff}$ vs. $\log g$ plot for stars with $-1.0 < [{\rm Fe/H}] < 0$ in LAMOST DR5.

Table 3
N-rich Field Stars Found in This Paper and Paper I

#	R.A.	Decl.	$T_{\rm eff}$[a] (K)	log g[a]	[Fe/H][a]	RV[a] (km s^{-1})	G_mag[b] (mag)	Distance[c] (kpc)	Note
1	260.961223	49.579740	4530.12	1.33	−1.32	−206.85	11.81	5.08	Paper II
2	272.312586	18.683633	4588.16	1.56	−1.18	−109.06	12.86	5.88	Paper II
3	126.054337	12.348258	5111.33	2.62	−1.25	−137.34	14.00	3.98	Paper II
..	...	...	...	...	...	...	...	...	...

Notes.
[a] From the LAMOST DR5 pipeline.
[b] *Gaia* DR2 *G*-band magnitudes.
[c] Distances determined by Chao Liu.
(This table is available in its entirety in machine-readable form.)

and the total percentage of these stars in our sample would increase to 2.4%. This percentage agrees with that of Martell & Grebel (2010), Martell et al. (2011), and Koch et al. (2019).

In order to study the evolutionary stages of our N-rich field star sample, we plot them along the parent sample in the $T_{\rm eff}$ versus $\log g$ space (Figure 1). It is evident that most of our N-rich field stars are located on the RGB, except for a few stars around $T_{\rm eff} \sim 5000$–5100 K and $\log g \sim 2.1$–2.2. What is the evolutionary stage of these stars? We also notice that the parent sample shows a feature around $T_{\rm eff} \sim 5250$–5400 K and $\log g \sim 2.5$–2.9, which intersects the RGB. To further explore this, we build two test samples with $-1.0 < [{\rm Fe/H}] < -0.5$ (test 1), and $-0.5 < [{\rm Fe/H}] < 0$ (test 2) from the LAMOST A-, F-, G-, K-type star catalog.[9] Figures 1 and 3 show that (1) the RGB is moving toward the red side as metallicity increases, as high metallicity increases opacity, which causes redder stars; (2) the typical red clump can be found for $-1.0 < [{\rm Fe/H}] < 0$ stars, while the feature on the lower left of the typical red clump is usually referred to as the secondary red clump. It is thought to be the result of a smaller He-core mass at ignition for stars with $2.2M_{\odot} < M < 3.0M_{\odot}$ (Pinsonneault et al. 2018). Therefore, the stars around $T_{\rm eff} \sim 5000$–5100 K and $\log g \sim 2.1$–2.2 are likely red clump stars.

To gain better visualization of the N-rich stars, we define δCH4300 as the CH4300 index value minus the mean of spectral indices at the $T_{\rm eff}$ of a given star (Table 2). A similar definition is also applied to CN3839. The N-rich stars clearly stand out in the δCN3839−δCH4300 plane (Figure 4). To define a control sample that represents the normal metal-poor field stars, we select stars that satisfy (1) $-0.05 < \delta{\rm CN3839} < 0.05$, (2) $-0.05 < \delta{\rm CH4300} < 0.05$ (the magenta box in Figure 4), and (3) $4000 < T_{\rm eff} < 5000$ K. In total, 1527 stars are selected. We will compare chemical and kinematic properties of N-rich field stars with those of the control sample to discuss their possible origins.

3. Chemical Abundances

The idea of "chemical tagging" (Freeman & Bland-Hawthorn 2002) envisages chemical abundances as labels for a given star which tell its evolution history and may be used as tracers to help us constrain its birth environment. In this sense, chemical abundances are crucial to understand the N-rich star origins.

[9] $T_{\rm eff}$, $\log g$, and SNR selection criteria are the same as those of our parent sample.

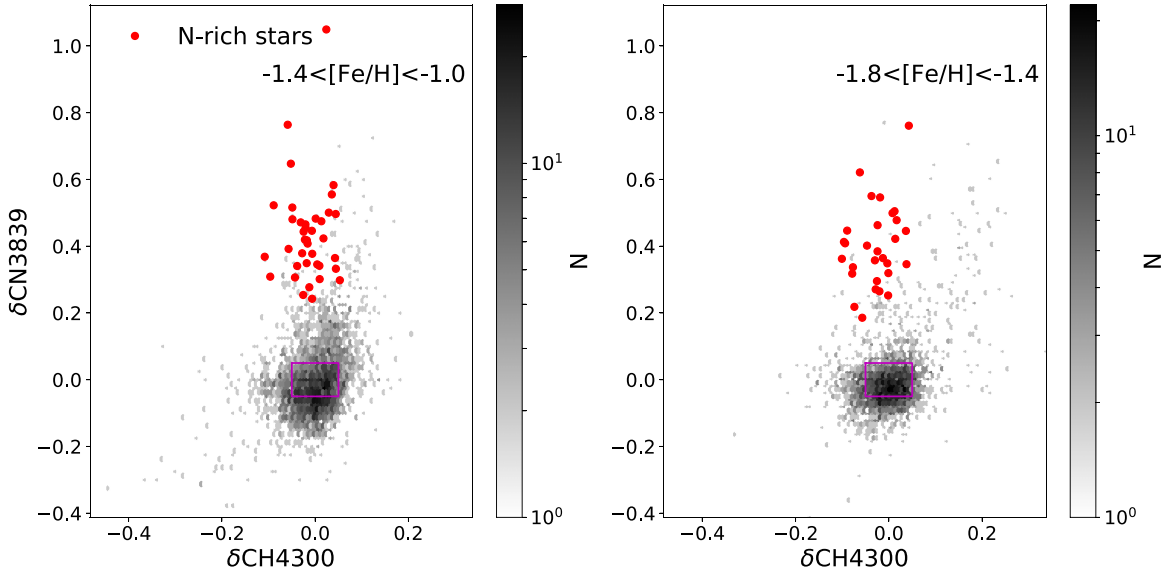

Figure 4. The δCN3839 vs. δCH4300 plot. The left panel includes more metal-rich stars, while the right panel includes more metal-poor stars. The N-rich field stars are labeled as red symbols. The grayscale map indicates the number density of metal-poor field stars. A sample of normal metal-poor field stars are selected based on their δCH4300 and δCN3839 indices outlined by the magenta box.

Table 4
Common Stars between Our N-rich Field Star Sample and APOGEE DR14

APOGEE_ID	$T_{\rm eff}$[a] (K)	log g[b]	[Fe/H][c]	[C/Fe]	[N/Fe]	[O/Fe]	[Mg/Fe]	[Al/Fe]	[Si/Fe]	[Ce/Fe]	Note
2M12561260+2804017	4848.65	1.87	−1.30	...	1.10	0.62	0.17	−0.04	0.24	0.59	Paper I
2M13233152+4931144	4778.95	1.89	−1.10	−0.41	0.97	0.39	0.21	0.19	0.19	0.09	Paper I
2M19112945+4626140	4867.39	1.80	−1.53	−0.22	1.47	0.54	0.39	0.99	0.44	0.41	Paper II
2M12512544+4258507	4753.45	2.26	−0.89	0.02	1.54	0.38	0.56	0.65	0.45	0.92	Paper II
2M19004420+4421082	4823.72	2.05	−0.98	−0.49	1.39	0.38	0.22	0.31	0.28	0.56	FT19
2M12010401-0058306	4880.99	2.25	−1.06	0.12	1.40	0.59	0.29	0.12	0.33	0.92	FT19
2M15535831+4333280	4656.55	1.58	−1.29	...	0.74	0.13	−0.42	1.07	0.51	0.32	FT19

Notes.
[a] Photometric $T_{\rm eff}$.
[b] Determined from 10 Gyr isochrones.
[c] ASPCAP values. Other abundances are derived using BACCHUS.

Despite being observationally more expensive, high-resolution spectra give more accurate chemical abundances. Thus, we seek help from high spectral resolution surveys, like APOGEE (Majewski et al. 2017). After cross-matching with the APOGEE DR14 database, we find 97 common stars in the control sample and 5 common stars in our N-rich star sample. APOGEE provides up to more than 20 elemental abundances (Holtzman et al. 2015) with the APOGEE Stellar Parameter and Chemical Abundances Pipeline (ASPCAP; García Pérez et al. 2016). While ASPCAP results are statistically reliable to 0.1 dex for several elements (Holtzman et al. 2015), caution should be taken when using ASPCAP results for individual stars (e.g., Schiappacasse-Ulloa et al. 2018), especially for metal-poor stars (below $[{\rm Fe/H}] = -1.4$ dex). Given that accurate chemical abundance derivation is computationally expensive, we plan to (1) use the ASPCAP results of these 97 common stars in the control sample without examining the details of each spectrum, but we mainly discuss their statistical mean and standard deviation values; and (2) derive detailed chemical abundances for common stars in the N-rich field star sample. It turns out that three of the five N-rich common stars are listed in Fernández-Trincado et al. (2019a, FT19). In this paper, we use the chemical abundances given by FT19 and apply the same procedure for deriving chemical abundances with photometric $T_{\rm eff}$ to the other two APOGEE-LAMOST common stars. We also include the two N-rich field stars with APOGEE spectra from Paper I.

Why are there four N-rich field stars observed by APOGEE but not included in FT19? It turns out that they are either outside the metallicity range selected in FT19, or right on the border that separates N-rich and normal field stars in FT19. Furthermore, we also check for common stars in Carretta et al. (2010a), Martell & Grebel (2010), Martell et al. (2011, 2016), Ramírez et al. (2012), Lind et al. (2015), Fernández-Trincado et al. (2016, 2017), and Schiavon et al. (2017). No overlap is found; therefore, we are presenting 53 newly identified N-rich stars in this work.

Briefly speaking, we first calculate the photometric $T_{\rm eff}$ with the $J_{\rm 2MASS}-K_{s,\rm 2MASS}$ color using the correlation of González Hernández & Bonifacio (2009), where the color is extinction corrected using the $E(B–V)$ provided by the APOGEE team. Photometric $\log g$ are estimated from 10 Gyr PARSEC isochrones with ASPCAP [Fe/H] (Table 4). Then, we estimate the chemical abundances using the Brussels Automatic Stellar Parameter (BACCHUS) code (Masseron et al. 2016). Readers

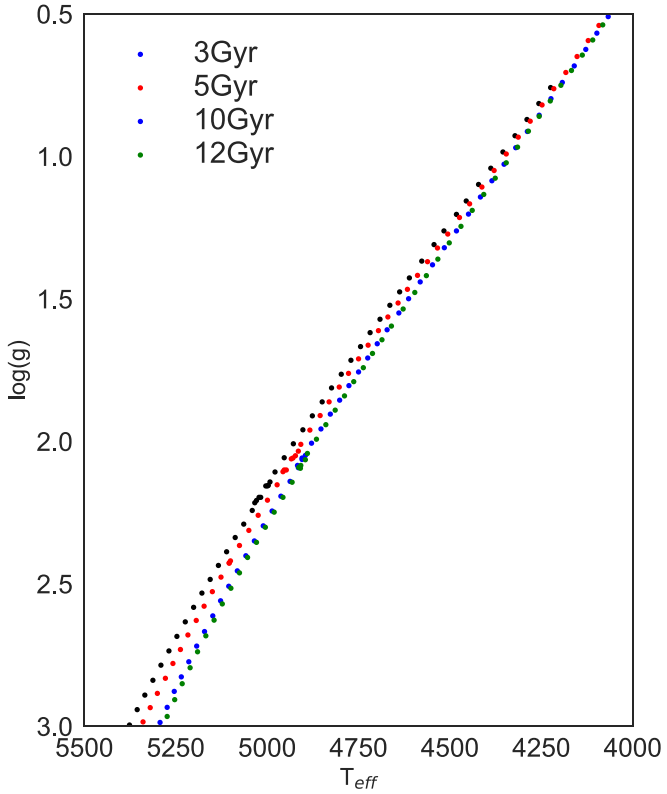

Figure 5. $T_{\rm eff}$ vs. $\log g$ plot of PARSEC isochrones with [Fe/H] = −1.3. Isochrone ages are 3 Gyr (black dots), 5 Gyr (red dots), 10 Gyr (blue dots), and 12 Gyr (green dots), respectively.

are referred to Tang et al. (2018) and FT19 for a detailed description about how we set up the BACCHUS code to compute chemical abundances. The results from the BACCHUS code are listed in Table 4. It is worth noticing that when [C/Fe] is too weak to determine a reasonable value (two out of the seven common stars), the associated [N/Fe] is in fact an upper limit. This is related to how we determine the C, N, and O abundances: we first derive ^{16}O abundances from ^{16}OH lines, then derive ^{12}C from ^{12}C^{16}O lines and ^{14}N from ^{12}C^{14}N lines. If the ^{12}C^{16}O lines are too weak, then we fix [C/Fe] to solar value, so the associated [N/Fe] should be interpreted as an upper limit and used with caution. There is concern about adopting 10 Gyr isochrones to evaluate our $\log g$, which may propagate errors to our abundance measurements. We download 3, 5, 10, and 12 Gyr isochrones with a typical metallicity of our sample: [Fe/H] = −1.3 from the PARSEC isochrone website.[10] The $\log g$ of different age isochrones in fact vary less than 0.1 dex at a given $T_{\rm eff}$ (Figure 5). This uncertainty in $\log g$ is much less than the $\log g$ uncertainty that we assume in FT19 and this paper (0.36 dex). Therefore, the abundance uncertainties caused by adopting different age isochrones are negligible compared to the uncertainties presented in Table 3 of FT19.

The BACCHUS-derived chemical abundances for our N-rich field stars and the ASPCAP-derived chemical abundances for the control sample are shown in Figure 6. On the upper-left panel, as we have demonstrated in Paper I, we find that normal metal-poor field stars are going through the so-called extra mixing (Iben 1967; Gratton et al. 2000) and our N-rich field stars are clearly above this sequence. Therefore, the N enrichment cannot be explained by the classical extra-mixing theory. A revision of the extra-mixing theory, or a new nucleosynthetic process that can produce very high N abundances, is needed. Two issues concerning the data reduction may complicate our discussion here: first, the N abundances derived by ASPCAP for APOGEE DR14 do not reach [N/Fe] > 1.0, due to the limited grid of models (Masseron et al. 2019); second, ^{12}C^{14}N spectral features in the APOGEE spectra become weak for stars with high temperature. For example, Masseron et al. (2019) suggested that [N/Fe] for stars with $T_{\rm eff}$ above 4600 K are mostly upper limits. To prove that our common APOGEE N-rich field stars are truly N enhanced, we show the APOGEE spectra of our N-rich field stars (without the [N/Fe] upper limits) in Figure 7. We center the spectra on the regions around the ^{12}C^{14}N band to visualize the spectral features. Clearly, all of the N-rich field stars show stronger spectral absorption of the ^{12}C^{14}N band, compared to other normal stars with similar stellar parameters. Our LAMOST-APOGEE common stars are bona fide N-rich field stars. This demonstrates our ability to select bona fide N-rich field stars from low-resolution LAMOST spectra and the purity of our N-rich field star sample.

On the upper-right panel, the N-rich field stars show similar, or even slightly higher, O abundances to other normal metal-poor field stars. Classical extra mixing is believed to affect C and N yields but not the C+N+O yields (Masseron et al. 2019). The C+N+O abundance sum for our five N-rich field stars with complete C, N, and O abundances is 8.44 ± 0.23, while for other normal metal-poor field stars, it is 7.64 ± 0.29. To minimize the effect of metallicity, we also compute the [C+N+O/Fe] for both samples. It is 0.68 ± 0.11 for N-rich field stars and 0.20 ± 0.13 for normal metal-poor field stars. Therefore, our N-rich field stars clearly have higher C+N+O yields compared to normal metal-poor field stars. This supports our above statement that the classical extra-mixing theory cannot explain the N enhancement that we found. As discussed in several recent literature (Villanova et al. 2010; Yong et al. 2015; Masseron et al. 2019), whether GC stars of different generations show distinct C+N+O yields is still unclear; even for the same GC (NGC 1851), whether the two generations show different C+N+O abundance sums is still inconclusive (Villanova et al. 2010; Yong et al. 2015). Thus, directly linking the different C+N+O abundance sum of our N-rich field stars compared to normal metal-poor field stars with the GC escapee scenario is still premature.

On the lower-left panel, we find that the [Al/Fe] of N-rich field stars are clearly higher than those of the control sample. Some can even reach [Al/Fe] ∼ 1. [Mg/Fe] are generally enhanced to a level of about 0.3 dex for both samples, consistent with their metal-poor halo star nature. An exception is found in 2M15535831+4333280, where [Mg/Fe] is as low as −0.42 dex. This star has been presented in FT19, and similar Mg-depleted N-rich field stars were also discussed in Fernández-Trincado et al. (2016, 2017). N-rich field stars showing Mg depletion are in fact rare, but whether Mg-depleted and Mg-enhanced N-rich field stars have common origins is still unclear. On the lower-right panel, the [Si/Fe] of N-rich field stars are scattered around 0.2–0.5 dex, generally consistent with other normal metal-poor field stars. Finally, we notice that the s-process element ([Ce/Fe]) abundances of two N-rich field stars are large (∼0.9 dex), pointing to a possible Asymptotic Giant Branch (AGB)-enriched scenario (Section 5.3). We are aware of the limited sample size of our N-rich stars with high-resolution chemical abundances, and a campaign to obtain high-resolution spectra for 20–30 N-rich field stars is on the way.

[10] http://stev.oapd.inaf.it/cgi-bin/cmd

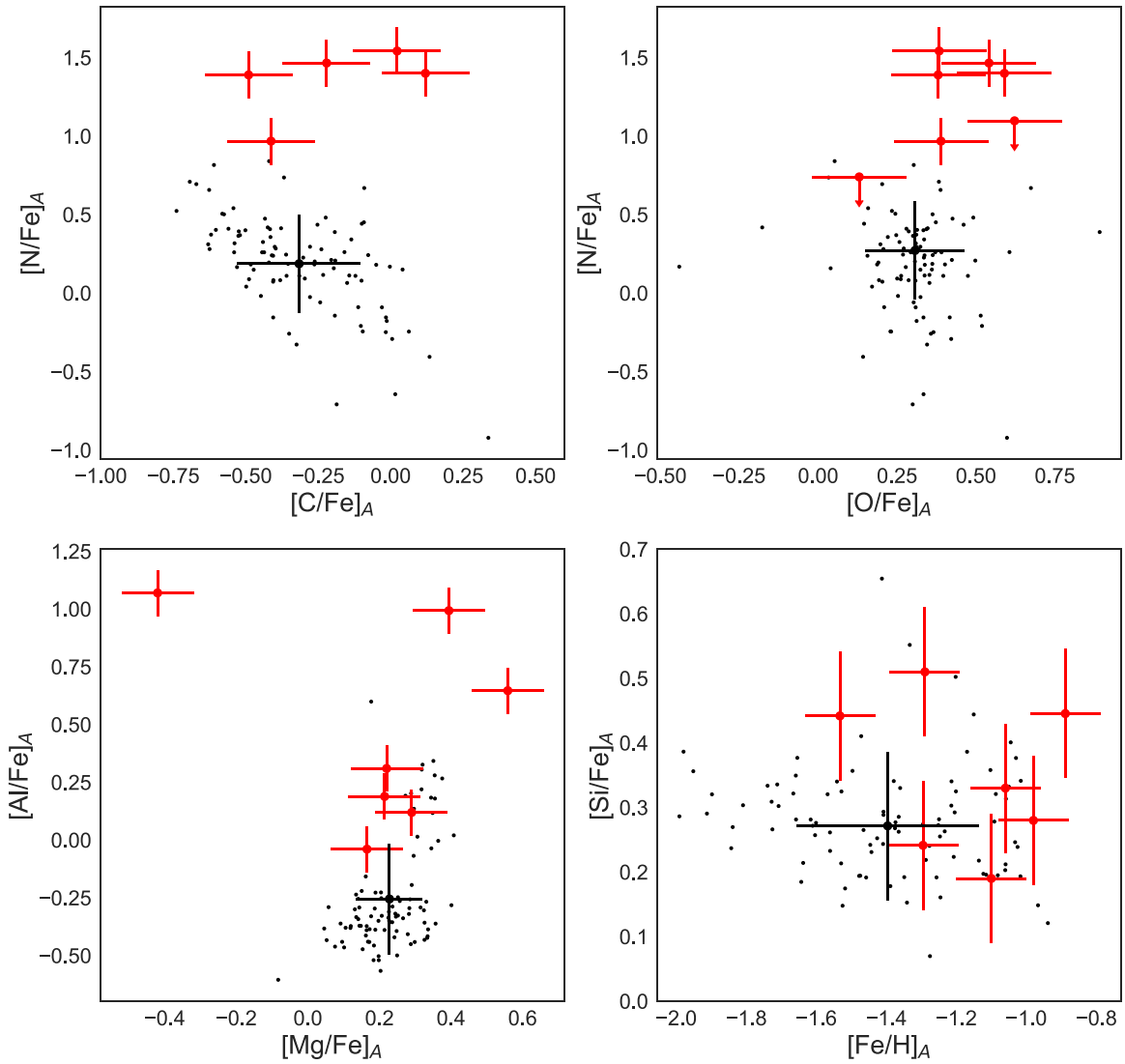

Figure 6. Chemical abundances derived from APOGEE near-IR spectra. The N-rich field stars commonly observed by LAMOST and APOGEE (DR14) are labeled by red symbols, where the associated error bars indicate the measurement uncertainties. The chemical abundances of the N-rich field stars are derived using the BACCHUS code. The normal metal-poor field stars commonly observed by LAMOST and APOGEE (DR14) are labeled as black dots. Their chemical abundances are given by ASPCAP. The black error bars indicate their mean and standard deviations.

4. Tracking Orbits

As stars travel through the MW gravitational potential, their orbital energy and angular momentum are generally conserved for a few gigayears, given the slowly varying MW gravitational potential. The orbital parameters of our N-rich field stars, especially when compared with normal metal-poor field stars, may reveal their unknown past. To provide a comprehensive dynamical study of our sample, we simulate the Galactic orbits in a 3D steady-state gravitational potential model for the Galaxy, modeled as the sum of axisymmetric and nonaxisymmetric components. The axisymmetric component is made up of the superposition of many composite stellar populations belonging to the thin disk (seven stellar subpopulations with ages ranging between 0.15 and 10 Gyr), where the density profile of each component follows the Einasto laws (Einasto 1979) and is observationally constrained as presented in Robin et al. (2003). The model also considers the contribution by two thick disks (with ages of 10 and 11 Gyr) whose profiles follow sech^2 laws similar to those presented in Robin et al. (2014, and an interstellar matter (ISM) component with density profile presented in Robin et al. (2003). The model also correctly accounts for the underlying stellar halo, modeled by a Hernquist profile as already described in Robin et al. (2014). The nonaxisymmetric component is modeled by a "boxy/peanut" bar structure whose density profile is observationally constrained from 2MASS data (see Robin et al. 2012), with assumed mass, present-day orientation, and pattern speeds within observational estimates: bar mass -1.0×10^{10} $M_{\odot}$ (Portail et al. 2017), angle $-20°$ (present-day angular offset from the Galactic x-axis in the direction of rotation), and $\Omega_{\mathrm{bar}}-33$ to 53 km s^{-1} kpc (in increments of 10 km s^{-1} kpc, which has a corotation radius of ~5.5–6.5 kpc) in line with Fernández-Trincado (2017), respectively. All of these stellar components are surrounded by an isothermal dark matter halo component with a density mass presented in Robin et al. (2003). It is important to note that the literature listed here indicates the origin of the density profiles of our model, but the mathematical functions associated with the gravitational potential ($\Phi(x, y, z)$) will be presented for the first time in a forthcoming paper by J. G. Fernández-Trincado et al. (2020, in preparation). Efforts are underway to provide our code

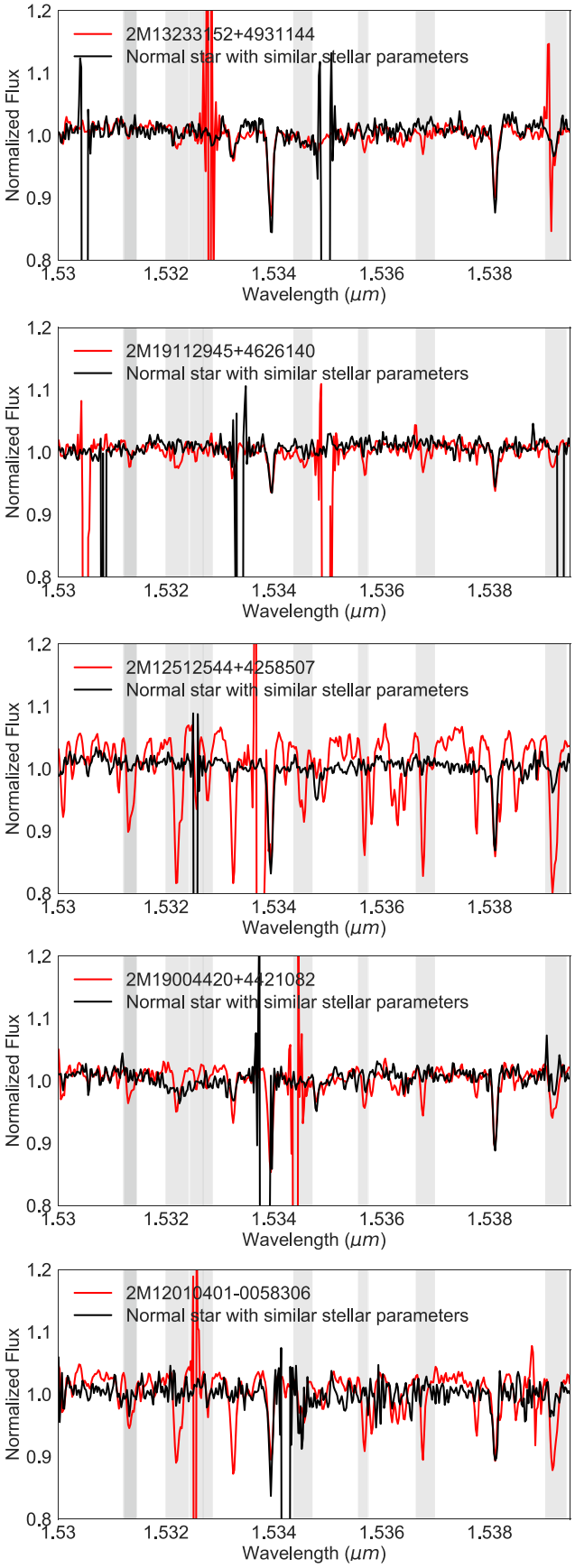

Figure 7. APOGEE spectra covering spectral regions around the $^{12}C^{14}N$ band (gray vertical bands). The N-rich field stars are labeled in red, while other normal stars with similar stellar parameters are shown in black.

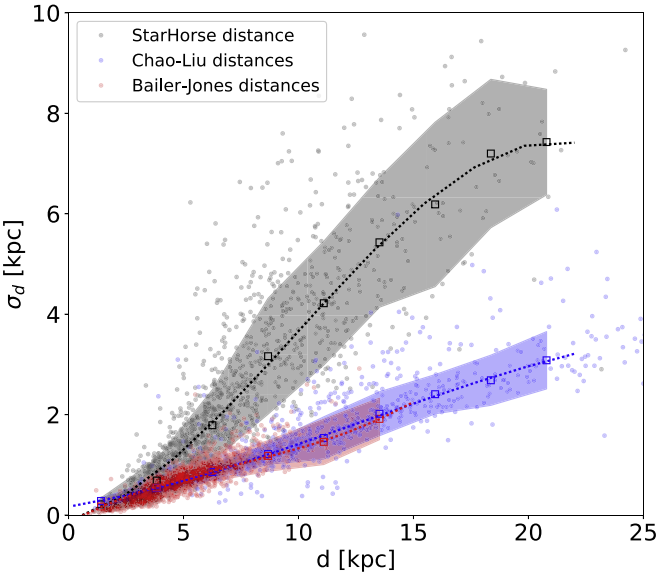

Figure 8. Distance error as a function of distance value given by three different methods for all N-rich field stars and normal metal-poor field stars. LC distances are labeled by blue dots, SH distances by gray dots, BJ distances by red dots. The mean errors at given distances and the associated 1σ uncertainty regions are shown as dashed lines and shaded regions. (See text.)

to the community by running it on a public server (https://gravpot.utinam.cnrs.fr).

For the Galactic orbits, we adopt a solar position of $R_\odot = 8.3$ kpc, $Z_\odot = 11$ pc, local kinematic parameters of $V_{\rm LSR} = 239\,{\rm km\,s^{-1}}$ (for the motion of the local standard of rest) and $[U,\ V,\ W]_\odot = [-11.10, -12.24,\ 7.25]$ km s^{-1}, in line with Brunthaler et al. (2011). We use a right-handed, Cartesian Galactocentric coordinate system, where the X-axis is oriented toward $l = 180°$, the Y-axis is oriented toward $l = 270°$, and the disk rotates toward $l \sim 90°$. For the computation of Galactic orbits, we have employed a simple Monte Carlo approach and the Runge–Kutta algorithm of seventh–eighth order. The uncertainties in the input data (e.g., α, δ, distance, proper motions, and line-of-sight velocity errors) were randomly propagated as 1σ variations in a Gaussian Monte Carlo resampling. For each star, we computed a thousand orbits, computed backward in time during 3 Gyr. The average value of the orbital elements was found for our 1000 realizations, with uncertainty ranges given by the 16th and 84th percentile values.

The input data for the Galactic model—distances, RVs, and absolute proper motions—are retrieved from the most recent survey results. We use absolute proper motions from the latest *Gaia* DR2 (Gaia Collaboration et al. 2018; Katz et al. 2019) and RVs from LAMOST. The typical uncertainty of LAMOST RVs is $4\,{\rm km\,s^{-1}}$, while the typical uncertainty of absolute proper motions is $0.05\,{\rm mas\,yr^{-1}}$. We compare distances derived from three different methods: (1) Bayesian spectrophotometric distances with no assumptions about the underlying populations (Carlin et al. 2015), hereafter LC distances (led by Chao Liu); (2) Bayesian spectrophotometric distances with flexible Galactic stellar-population priors (Queiroz et al. 2018), hereafter SH (StarHorse) distances; and (3) Bayesian *Gaia* DR2 parallax-based distances (Bailer-Jones et al. 2018), hereafter BJ distances. We compare the distance errors of the aforementioned methods in Figure 8. We notice that (1) the uncertainties of SH distances are the largest among the three, and (2) BJ distances and LC

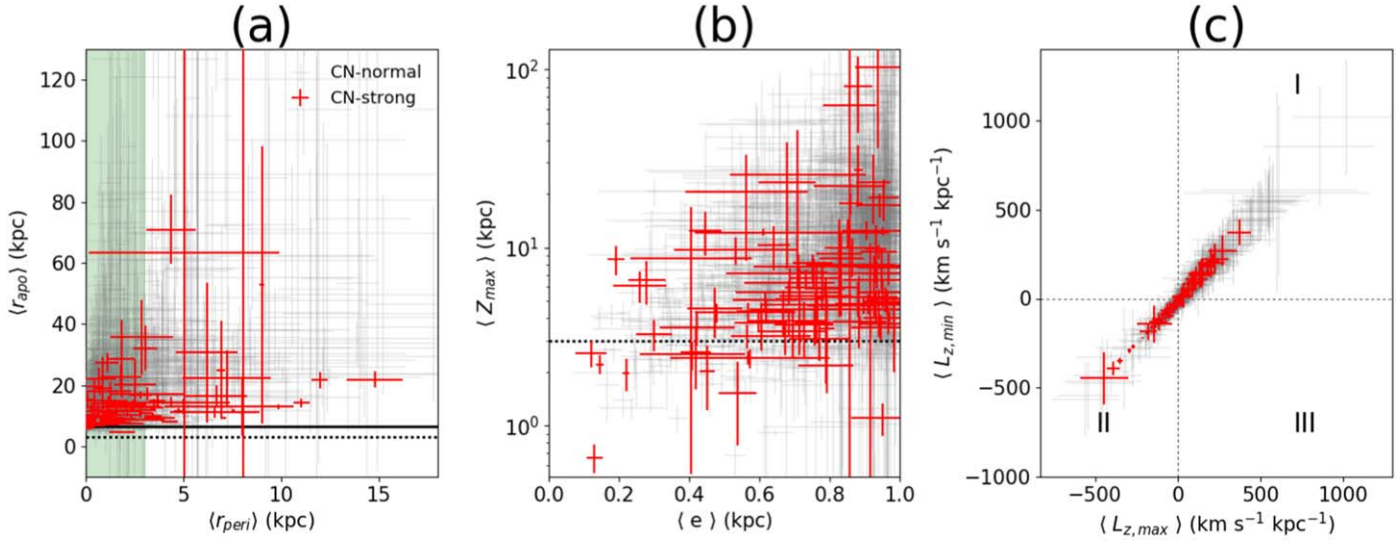

Figure 9. The plots of average values of orbital parameters over 1000 realizations for the N-rich field stars (red symbols) and the control sample (gray symbols). The parameters include perigalactic radius ($\langle r_{\rm peri}\rangle$), the apogalactic radius ($\langle r_{\rm apo}\rangle$), the orbital eccentricity ($\langle e\rangle$), the maximum vertical amplitude ($\langle Z_{\rm max}\rangle$), the minimum angular momentum in z-direction ($\langle L_{z,\rm min}\rangle$), and the maximum angular momentum in z-direction ($\langle L_{z,\rm max}\rangle$). The error bars indicate uncertainty ranges given by the 16th and 84th percentile values.

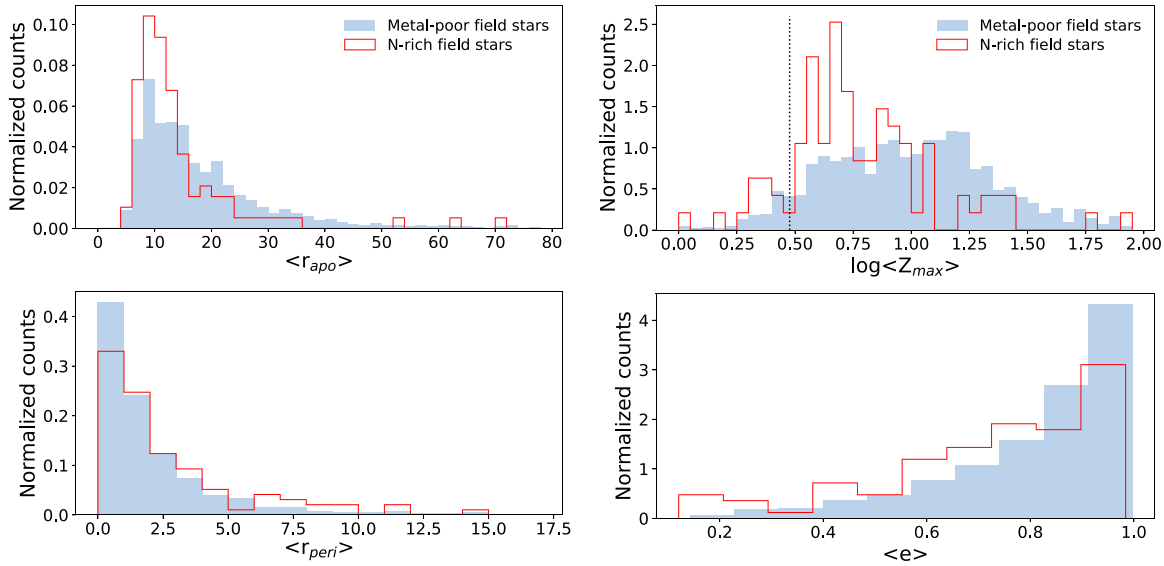

Figure 10. The $\langle r_{\rm apo}\rangle$ (upper-left panel), $\langle r_{\rm peri}\rangle$ (lower-left panel), log $\langle Z_{\rm max}\rangle$ (upper-right panel), and $\langle e\rangle$ (lower-right panel) distribution histograms of N-rich field stars (red histograms) and normal metal-poor field stars (gray histograms).

distances have comparable uncertainties for nearby stars (distance less than 7 kpc), but the number of stars with distance greater than 7 kpc is almost negligible if BJ distances are assumed. Because BJ distances are based on parallaxes from *Gaia* DR2, if a star is too far away, the parallax becomes too small to be detectable. Currently, the parallax-based distances of stars farther than ∼5 kpc are expected to be dominated by their assumed priors. Therefore, we adopt LC distances to compute stellar orbits in this work.

From the integrated set of orbits, we compute (1) the perigalactic radius, $r_{\rm peri}$, (2) the apogalactic radius, $r_{\rm apo}$, (3) the orbital eccentricity, defined as $e = (r_{\rm apo} - r_{\rm peri})/(r_{\rm apo} + r_{\rm peri})$, and (4) the maximum vertical amplitude, $Z_{\rm max}$.

A long list of studies in the literature has presented different ranges for the bar pattern speeds (Portail et al. 2017; Monari et al. 2017a, 2017b). For our computations, we assume three pattern speeds: $\Omega_{\rm B} = 33$, 43, and 53 km s^{-1} kpc^{-1}. Because most of our stars are located in the halo, we do not expect substantial differences in our orbital parameters when adopting different pattern speeds, as we found in Paper I. Therefore, we adopt $\Omega_{\rm B} = 43$ km s^{-1} kpc^{-1} in the following study.

In this work, we have combined the N-rich field stars in this paper and Paper I to form a ∼100 star sample. This is the largest homogeneous N-rich field star sample with kinematic and orbital information. Readers are referred to Paper I for the classical Toomre diagram. In this work, we use histograms to better visualize the distribution differences between samples. Figures 9 and 10 show that our N-rich field stars have smaller $\langle r_{\rm apo}\rangle$, $\langle e\rangle$, and $\langle Z_{\rm max}\rangle$ compared to the control sample. (1) The N-rich field star sample and the control sample have no star with $\langle r_{\rm apo}\rangle$ less than 3 kpc, indicating no star is constrained inside the bulge (Barbuy et al. 2018). (2) Two samples have

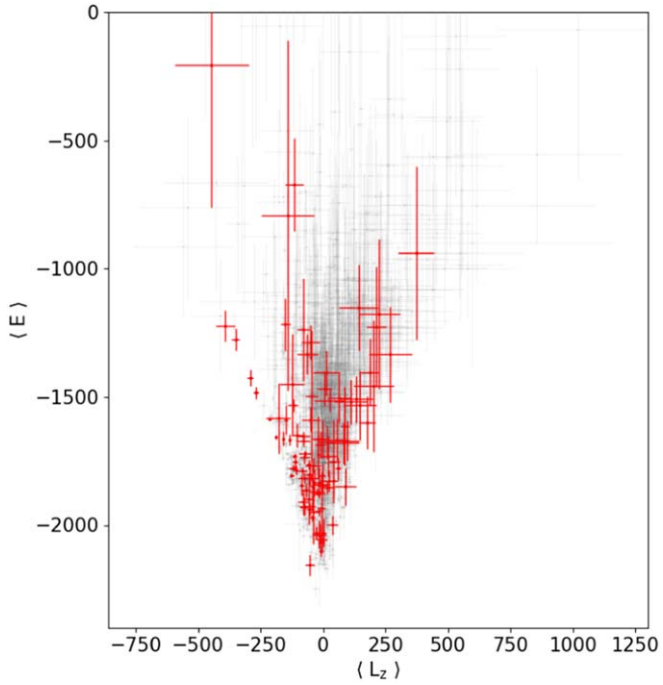

Figure 11. The N-rich field stars (red) and normal metal-poor field stars (gray) in the integral of motion space.

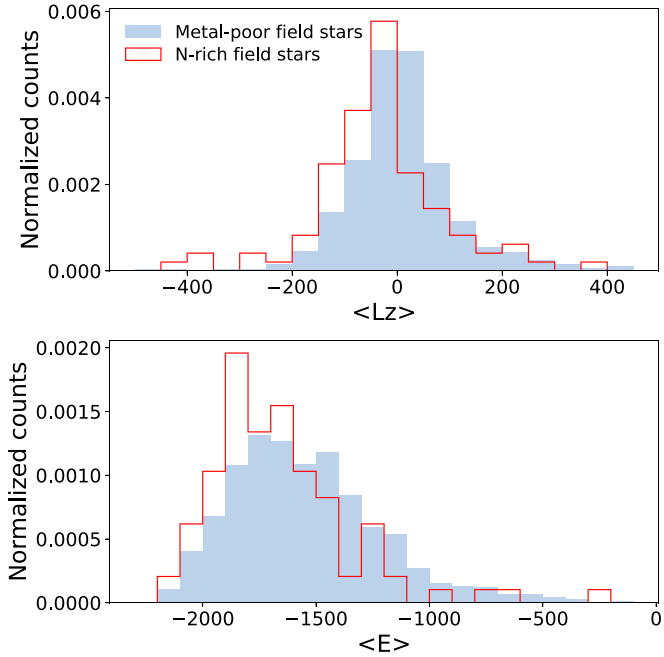

Figure 12. $\langle E\rangle$ (upper panel) and $\langle L_z\rangle$ (lower panel) distribution histograms of N-rich field stars (red histograms) and normal metal-poor field stars (gray histograms).

more stars toward high eccentricity. (3) The two-sample Kolmogorov–Smirnov (K–S) test indicates that the probability that the $\langle Z_{\rm max}\rangle$ (and $\langle r_{\rm apo}\rangle$) of the two samples are drawn from the same parent population is lower than 10^{-5}. Assuming the thick-disk edge is ∼3 kpc (Carollo et al. 2010, black dotted lines in the upper-right panel of Figure 10) and taking the above observational evidence into account, we conclude that (1) both our N-rich field stars and the control sample stars are mostly halo stars and (2) our N-rich field stars are located closer to the inner halo compared to the control sample. A similar conclusion was also found by Carollo et al. (2013).

The total orbital energy and z-direction angular momentum of a star should be conserved in a time-invariant gravitational potential. Therefore, the integral of motion space (IoM; E versus L_z) is a smoking gun to trace the history of a star. Because GravPot16 employs an axis-asymmetric Galactic potential, with a slowly rotating bar in the center of our Galaxy, the total orbital energy and z-direction angular momentum of a star is no longer constant. In this work, we use the mean of total orbital energy ($\langle E\rangle$) and the mean of the z-direction angular momentum ($\langle L_z\rangle$) over integration time to construct the IoM space. To ensure that we draw solid conclusions from the IoM space, we also simulate the orbits in an axisymmetric potential. After comparing the results from the two Galactic potential models (e.g., Figure 11), we find that the differences in the IoM space is negligible, mainly because our stars are mostly located in the halo. Thus, the following conclusions that we draw from the IoM space are valid in both axisymmetric and axis-asymmetric Galactic potential models.

Figure 11 shows the IoM space for N-rich field stars and the control sample. The detailed distributions of $\langle E\rangle$ and $\langle L_z\rangle$ can be found in Figure 12. We point out that our $\langle L_z\rangle$ is slightly different from some other studies: positive sign means retrograde and negative sign means prograde. This is related to the above-mentioned Galactocentric coordinate system that we use in this work. Compared with the locations of different Galactic components in the IoM space (e.g., Massari et al. 2019), Figure 11 suggests that except for a small portion of stars located in the thick disk, most of our N-rich field stars are halo stars, which is consistent with what we find using $\langle Z_{\rm max}\rangle$ (Figure 10). Furthermore, Figure 12 reveals that N-rich field stars have smaller $\langle E\rangle$ (less energetic orbits) and $\langle L_z\rangle$ (more prograde orbits) compared with the control sample. The two-sample K–S test indicates that the probability that $\langle E\rangle$ (and $\langle L_z\rangle$) of the two samples are drawn from the same parent population is lower that 10^{-4}. The less energetic and more prograde orbits of our N-rich field stars again suggest they are inner-halo stars.

5. Discussion

5.1. Li Abundances

Li is a volatile element that can be easily destroyed in a high-temperature environment. As a star evolves along the RGB, the Li abundance sharply decreases as the star goes through the first dredge-up. After the star reaches the RGB bump, the classical extra-mixing process is suggested to destroy Li and C, and to generate N (e.g., Iben 1967; Gratton et al. 2000; Charbonnel & Zahn 2007; Charbonnel & Lagarde 2010). But as we have discussed in Paper I and in this paper, the N abundances of our N-rich field stars are clearly larger than the values predicted by classical extra mixing. Another nuclear process that can produce higher N abundances is needed.

Interestingly, the discovery of Li-rich stars has also defied the classical extra-mixing process, and researchers have modified the classical extra-mixing process into nontraditional ones, e.g., enhanced extra mixing or asymmetric extra mixing (Yan et al. 2018). The possible discovery of a few N-rich stars in a sample of Li-rich stars (L. Sbordone 2020, private communication) has inspired us to search for possible Li-rich

Table 5
N-rich Field Stars with Possible Li Enrichment

#	R.A.	Decl.	RV (km s^{-1})	$T_{\rm eff}$ (K)	log g	[Fe/H]	A(Li)	Note
1	253.944305	21.655846	−151.44	4717.13	1.677	−1.450	1.160	Paper II
2	197.656036	−6.979531	−12.78	5173.49	2.754	−1.402	1.722	Paper II
3	268.058044	26.255920	−288.09	5065.61	2.783	−1.279	1.414	Paper II
4	122.120483	1.946907	127.52	4984.40	2.071	−1.534	1.382	Paper II
5	197.834381	2.999973	22.19	4955.84	2.345	−1.245	1.414	Paper II
6	317.852325	−2.385546	−0.86	5058.77	1.871	−1.069	1.65	Paper I
7	247.988815	39.067295	−59.71	4988.19	2.804	−0.664	1.518	Paper I

stars in our sample. Do they have some sort of channel to keep both N and Li at a high level? We determine the Li abundances following the procedure given in Gao et al. (2019). Briefly speaking, the Li abundance is derived from the template-matching method to a pure giant sample which contains over 800,000 giant stars from LAMOST data. The templates are synthesized using the SPECTRUM code, based on the stellar parameters provided by the LAMOST pipeline. The intervals of the grid templates are set to be 100 K, 0.25, 0.20, and 0.10 dex for $T_{\rm eff}$, log g, [Fe/H], and Li abundance, respectively. The abundance is determined by fitting a curve to the chi-square array and finding its minimum. Finally, a by-eye inspection is used to double-check the matching result and eliminate the unreliable ones.

Generally speaking, most of the N-rich stars show A(Li) < 1.0,[11] suggesting that the coexistence of high N and high Li seems to be unlikely. However, we do notice a few possible candidates with higher Li abundances than normal stars (Table 5). Because it is relatively difficult to accurately determine Li abundances for stars with A(Li) < 1.5 using low-resolution LAMOST spectra, we leave a detailed discussion of these interesting stars after obtaining high-resolution optical spectra.

5.2. Galactic versus Extragalactic Origin

Starting from the 1990s, astronomers began to apprehend the varieties in the age–metallicity relation and predicted orbits of Galactic GCs (GGCs; Fusi Pecci et al. 1995; Mackey & Gilmore 2004; Forbes & Bridges 2010; Law & Majewski 2010). GGCs are suggested to be separated into in situ population and accreted population (e.g., Forbes & Bridges 2010). Thanks to the unprecedented accuracy in proper motion and astrometry presented by *Gaia*, the accreted versus in situ theory for GGCs is rapidly developing (Massari et al. 2019; Myeong et al. 2019; Vasiliev 2019), based on not only the kinematics but also the chemical information from other spectroscopic surveys. The action-angle space and IoM space are suggested to efficiently isolate GCs from different progenitors. In this work, due to the uncertainties in determining distances to halo individual stars, directly linking N-rich field stars to current GGCs with only IoM space distribution (Figure 11) may overinterpret our data. However, we notice that GGCs are mainly located in the inner halo (e.g., Figure 5 of Vasiliev 2019), while our N-rich field stars are also mostly inner-halo stars. This generally supports the MW–GC interaction scenario, where inner-halo GGCs are prone to stronger dynamical interactions with the MW, and therefore higher possibility to lose (N-rich) stars to the field. In that sense, the Galactic 6D distribution of our bona fide sample of N-rich field stars is a strong observational evidence for galaxy–GC coevolution simulations.

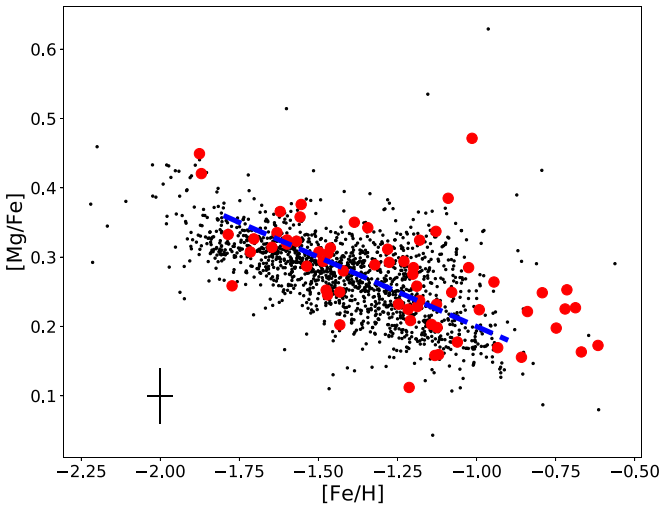

Figure 13. [Mg/Fe] vs. [Fe/H] plot. The N-rich field stars labeled by red dots. The normal metal-poor field stars are shown as small black dots. The line that separates accreted stars and in situ stars as proposed by Hayes et al. (2018) is the blue dashed line. The typical uncertainties of abundance measurements are shown in the bottom left as error bars.

On the other hand, because a number of GCs are accreted to our MW, if we assume that our N-rich field stars are dissolved from GCs, then we should be able to find both in situ and accreted stars in our N-rich field star sample. Hayes et al. (2018) showed that [Mg/Fe] versus [Fe/H] may be able to separate stars formed in situ or ex situ. Though our LAMOST spectra are low resolution, where a lot of element lines are blended, one can still derive chemical abundances with uncertainties of ∼0.1 dex for the most prominent lines, e.g., the Mg*b* line. Here we use the Mg abundances derived by a data-driven code, SLAM (Zhang et al. 2020), to investigate our N-rich field star sample and control sample. Figure 13 shows that our N-rich field star sample and the control sample are similarly distributed in the [Mg/Fe] versus [Fe/H] plane. The line that separates accreted stars and in situ stars proposed by Hayes et al. (2018) is labeled by the blue dashed line in the figure. We do not see a clear separation near the blue dashed line in our data, indicating that two samples consist of both in situ and accreted stars. Recently, Ostdiek et al. (2019) compiled a catalog of accreted stars with full 6D phase-space information and extended the catalog to stars with only 5D information using the machine-learning technique. We find 11 common stars between the 6D phase-space accreted star catalog and our N-rich field stars from Paper I and this paper. Four stars are labeled as accreted stars. With the caution of

[11] A(Li) = log($N_{\rm Li}/N_{\rm H}$)+12, where $N_{\rm Li}$ and $N_{\rm H}$ are the number densities of lithium and hydrogen, respectively.

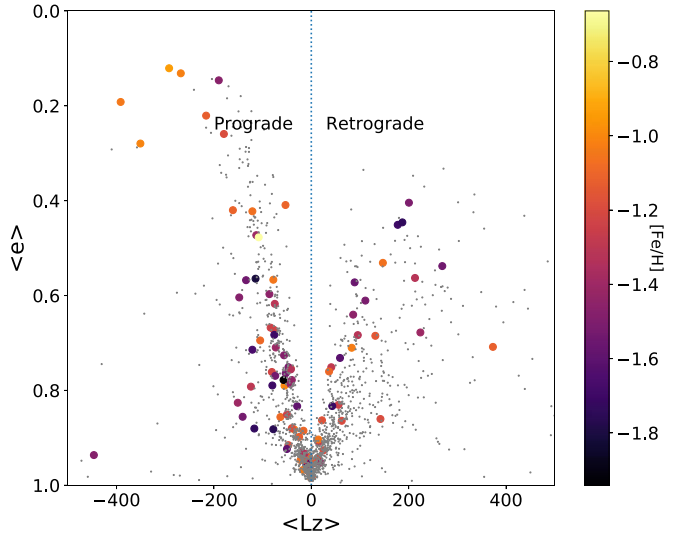

Figure 14. The $\langle e \rangle$ vs. $\langle L_z \rangle$ plot for N-rich field stars (color dots) and normal metal-poor field stars (gray dots).

small statistics (4 out of 11 stars), it seems that a substantial portion of our N-rich field stars may be accreted to the MW. The above-mentioned evidences seem to further strengthen the GC origin scenario of the N-rich field stars.

Savino & Posti (2019) compared GGCs and a population of CN-strong stars in terms of kinematics, e.g., IoM space distributions. They suggested that a group of low-circularity stars with [Fe/H] ~ -1 may come from the outer Galactic disk. Here we use eccentricity instead of circularity, given that high-circularity stars tend to have low eccentricity. We directly plot eccentricity as a function of $\langle L_z \rangle$ (using [Fe/H] as color) in Figure 14. Low-eccentricity stars tend to have more-circular orbits and higher angular momentum, for both the N-rich field star sample and the control sample. This trend seems to be continuous. The clustering at [Fe/H] ~ -1 for low-eccentricity stars as suggested by Savino & Posti (2019) is vaguely seen ($\sim$11 stars) in our work. If such group of N-rich field stars with disk-like kinematics and [Fe/H] ~ -1 do exist, their GC origin scenario may still hold, because there is evidence that support the existence of thick-disk GCs, e.g., Figure 4 of Massari et al. (2019) and NGC 5927 (Allen et al. 2008; Mura-Guzmán et al. 2018).

If N-rich field stars originated from existing/dissolved GCs, then a bona fide sample of N-rich field stars would be crucial to understand the formation and coevolution of the MW and GCs (e.g., E-MOSAIC; Kruijssen et al. 2019).

5.3. AGB-contaminated Materials

The recent discovery of a N-rich, mildly metal-poor ([Fe/H] $= -1.08$) giant star in a single-lined spectroscopic system by Fernández-Trincado et al. (2019b) has inspired the scenario that some N-rich metal-poor "field" stars may reside in binary systems, where the AGB companion stars have died out. A binary AGB companion scenario was also invoked by Simpson & Martell (2019) to explain a N-rich ([N/Fe] $> +2.5$), metal-poor ([Fe/H] < -2) star found in the globular cluster ESO280-SC06. According to nucleosynthetic theories (e.g., Masseron et al. 2010; Karakas & Lattanzio 2014), high N abundances can be seen in intermediate-mass AGB stars, where hot-bottom burning (HBB) can produce N at the expense of C.

On the other hand, several theories have been proposed to explain the chemically enriched populations in GCs, e.g., AGB ejecta (e.g., D'Ercole et al. 2008, 2010; Ventura et al. 2013), fast-rotating massive stars (Decressin et al. 2007), massive binaries (de Mink et al. 2009), supermassive stars (Denissenkov & Hartwick 2014), etc. However, none of them seem to explain all observational evidence of GCs (e.g., Bastian & Lardo 2018). In spite of its need for improvements, the AGB-ejecta scenario stands out for its ability to explain the observed N and Na (Al) enhancement and C and O (Mg) depletion in SG stars. In that scenario, the chemical peculiarity is attributed to the HBB-phase nucleosynthesis of AGB stars. Recently, Bekki (2019) proposed that the high-density building blocks of the Galactic bulge may also generate suitable AGB ejecta, which can explain the N enhancement of some bulge field stars.

There is one thing in common among these scenarios: AGB ejecta. Therefore, we may only be able to confirm the importance of AGB ejecta in N-rich field stars from the chemical point of view. In that sense, kinematic information is key to disentangle these three scenarios. To verify the binary AGB companion scenario demands further observational data, where light curves and RV changes are indicators of the presence of binary systems. However, the inner-halo-like orbits of our N-rich field stars seem to favor the GC scenario over the bulge scenario (Section 4).

6. Conclusion

Since the discovery of N-rich field stars, astronomers have proposed different scenarios to explain this phenomenon, including GCs, AGB binaries, the Galactic bulge, etc. A comprehensive bona fide sample with detailed chemical and kinematic information is needed to unveil the truth. In this paper, we have extended our search for N-rich field stars to LAMOST DR5, where we efficiently identified $\sim$100 such stars with CN–CH bands. We first investigate chemical abundances through seven common stars with APOGEE high-resolution spectra. The Mg, Al, and Si abundances of these common stars generally agree with that of GC-enriched stars, but it is still inconclusive for C, N, and O. On the other hand, the orbits of N-rich field stars show similar properties to inner-halo stars: lower $\langle Z_{\rm max} \rangle$, $\langle r_{\rm apo} \rangle$, $\langle L_z \rangle$, and $\langle E \rangle$ compared to normal metal-poor halo field stars. The kinematics of N-rich field stars and GCs seem to share similarities. The lack of multiepoch RV data prevents us from drawing conclusions on the binary AGB companion scenario. We are aware of the limited sample size of N-rich field stars with high-resolution spectra, from where we derived chemical abundances. To achieve a statistically significant conclusion, we plan to obtain high-resolution spectra for 20–30 N-rich field stars. Detailed chemical patterns and multiepoch RV data of a statistically significant sample of N-rich field stars will further constrain their formation scenarios.

We thank Luca Sbordone, Yue Wang, and Bryan Ostdiek for helpful discussions. We thank the anonymous referee for insightful comments. B.T. gratefully acknowledges support from the National Natural Science Foundation of China under grant No. U1931102 and support from the hundred-talent project of Sun Yat-sen University. J.G.F.-T. is supported by FONDECYT No. 3180210 and Becas Iberoam´erica Investigador 2019, Banco Santander, Chile. This research is supported by the National Natural Science Foundation of China under

grant Nos. 11603037 and 11973052. H.-L.Y. acknowledges support from Youth Innovation Promotion Association, CAS, and the support from the Astronomical Big Data Joint Research Center, co-founded by the National Astronomical Observatories. D.G. gratefully acknowledges support from the Chilean Centro de Excelencia en Astrofísica y Tecnologías Afines (CATA) BASAL grant AFB-170002. D.G. also acknowledges financial support from the Dirección de Investigación y Desarrollo de la Universidad de La Serena through the Programa de Incentivo a la Investigación de Académicos (PIA-DIDULS).

Guoshoujing Telescope (the Large Sky Area Multi-Object Fiber Spectroscopic Telescope LAMOST) is a National Major Scientific Project built by the Chinese Academy of Sciences. Funding for the project has been provided by the National Development and Reform Commission. LAMOST is operated and managed by the National Astronomical Observatories, Chinese Academy of Sciences. Funding for the GravPot16 software has been provided by the Centre National D'Etudes Spatiale (CNES) through grant 0101973 and the UTINAM Institute of the Universite de Franche-Comte supported by the Region de Franche-Comte and Institut des Sciences de l'Univers (INSU). Monte Carlo simulations have been executed on computers from the Utinam Institute of the Universite de Franche-Comte supported by the Region de Franche-Comte and Institut des Sciences de l'Univers (INSU).

ORCID iDs

Baitian Tang https://orcid.org/0000-0002-0066-0346
Chao Liu https://orcid.org/0000-0002-1802-6917
Qi Gao https://orcid.org/0000-0003-4972-0677
Jianrong Shi https://orcid.org/0000-0002-0349-7839
Douglas Geisler https://orcid.org/0000-0002-3900-8208

References

Allen, C., Moreno, E., & Pichardo, B. 2008, ApJ, 674, 237
Antoja, T., Helmi, A., Romero-Gómez, M., et al. 2018, Natur, 561, 360
Bailer-Jones, C. A. L., Rybizki, J., Fouesneau, M., Mantelet, G., & Andrae, R. 2018, AJ, 156, 58
Barbuy, B., Chiappini, C., & Gerhard, O. 2018, ARA&A, 56, 223
Bastian, N., & Lardo, C. 2018, ARA&A, 56, 83
Bekki, K. 2019, MNRAS, 490, 4007
Binney, J., & Schönrich, R. 2018, MNRAS, 481, 1501
Blanton, M. R., Bershady, M. A., Abolfathi, B., et al. 2017, AJ, 154, 28
Brunthaler, A., Reid, M. J., Menten, K. M., et al. 2011, AN, 332, 461
Carlin, J. L., Liu, C., Newberg, H. J., et al. 2015, AJ, 150, 4
Carollo, D., Beers, T. C., Chiba, M., et al. 2010, ApJ, 712, 692
Carollo, D., Martell, S. L., Beers, T. C., & Freeman, K. C. 2013, ApJ, 769, 87
Carretta, E., Bragaglia, A., Gratton, R., et al. 2010a, ApJL, 712, L21
Carretta, E., Bragaglia, A., Gratton, R. G., et al. 2010b, A&A, 516, A55
Charbonnel, C., & Lagarde, N. 2010, A&A, 522, A10
Charbonnel, C., & Zahn, J.-P. 2007, A&A, 467, L15
de Mink, S. E., Pols, O. R., Langer, N., & Izzard, R. G. 2009, A&A, 507, L1
Decressin, T., Charbonnel, C., & Meynet, G. 2007, A&A, 475, 859
Deng, L.-C., Newberg, H. J., Liu, C., et al. 2012, RAA, 12, 735
Denissenkov, P. A., & Hartwick, F. D. A. 2014, MNRAS, 437, L21
D'Ercole, A., D'Antona, F., Ventura, P., Vesperini, E., & McMillan, S. L. W. 2010, MNRAS, 407, 854
D'Ercole, A., Vesperini, E., D'Antona, F., McMillan, S. L. W., & Recchi, S. 2008, MNRAS, 391, 825
Einasto, J. 1979, in IAU Symp. 84, The Large-Scale Characteristics of the Galaxy, ed. W. B. Burton (Dordrecht: Reidel), 451
Eisenstein, D. J., Weinberg, D. H., Agol, E., et al. 2011, AJ, 142, 72
Fernández-Trincado, J. G. 2017, Phd Thesis, Université Bourgogne Franche-Comté 1, 74
Fernández-Trincado, J. G., Beers, T. C., Tang, B., et al. 2019a, MNRAS, 488, 2864
Fernández-Trincado, J. G., Mennickent, R., Cabezas, M., et al. 2019b, A&A, 631, A97
Fernández-Trincado, J. G., Robin, A. C., Moreno, E., et al. 2016, ApJ, 833, 132
Fernández-Trincado, J. G., Zamora, O., García-Hernández, D. A., et al. 2017, ApJL, 846, L2
Forbes, D. A., & Bridges, T. 2010, MNRAS, 404, 1203
Freeman, K., & Bland-Hawthorn, J. 2002, ARA&A, 40, 487
Fusi Pecci, F., Bellazzini, M., Cacciari, C., & Ferraro, F. R. 1995, AJ, 110, 1664
Gaia Collaboration, Brown, A. G. A., Vallenari, A., et al. 2018, A&A, 616, A1
Gao, Q., Shi, J.-R., Yan, H.-L., et al. 2019, ApJS, 245, 33
García Pérez, A. E., Allende Prieto, C., Holtzman, J. A., et al. 2016, AJ, 151, 144
Gilmore, G., Randich, S., Asplund, M., et al. 2012, Msngr, 147, 25
González Hernández, J. I., & Bonifacio, P. 2009, A&A, 497, 497
Gratton, R. G., Sneden, C., Carretta, E., & Bragaglia, A. 2000, A&A, 354, 169
Harbeck, D., Smith, G. H., & Grebel, E. K. 2003, AJ, 125, 197
Hayes, C. R., Majewski, S. R., Shetrone, M., et al. 2018, ApJ, 852, 49
Helmi, A., Babusiaux, C., Koppelman, H. H., et al. 2018, Natur, 563, 85
Holtzman, J. A., Shetrone, M., Johnson, J. A., et al. 2015, AJ, 150, 148
Ibata, R. A., Bellazzini, M., Malhan, K., Martin, N., & Bianchini, P. 2019a, NatAs, 3, 667
Ibata, R. A., Malhan, K., & Martin, N. F. 2019b, ApJ, 872, 152
Iben, I., Jr. 1967, ApJ, 147, 624
Karakas, A. I., & Lattanzio, J. C. 2014, PASA, 31, e030
Katz, D., Sartoretti, P., Cropper, M., et al. 2019, A&A, 622, A205
Khoperskov, S., Di Matteo, P., Gerhard, O., et al. 2019, A&A, 622, L6
Koch, A., Grebel, E. K., & Martell, S. L. 2019, A&A, 625, A75
Kruijssen, J. M. D., Pfeffer, J. L., Reina-Campos, M., Crain, R. A., & Bastian, N. 2019, MNRAS, 486, 3180
Law, D. R., & Majewski, S. R. 2010, ApJ, 718, 1128
Lind, K., Koposov, S. E., Battistini, C., et al. 2015, A&A, 575, L12
Luo, A.-L., Zhao, Y.-H., Zhao, G., et al. 2015, RAA, 15, 1095
Mackey, A. D., & Gilmore, G. F. 2004, MNRAS, 355, 504
Majewski, S. R., Schiavon, R. P., Frinchaboy, P. M., et al. 2017, AJ, 154, 94
Malhan, K., Ibata, R. A., & Martin, N. F. 2018, MNRAS, 481, 3442
Martell, S. L., & Grebel, E. K. 2010, A&A, 519, A14
Martell, S. L., Shetrone, M. D., Lucatello, S., et al. 2016, ApJ, 825, 146
Martell, S. L., Smolinski, J. P., Beers, T. C., & Grebel, E. K. 2011, A&A, 534, A136
Massari, D., Koppelman, H. H., & Helmi, A. 2019, arXiv:1906.08271
Masseron, T., García-Hernández, D. A., Mészáros, S., et al. 2019, A&A, 622, A191
Masseron, T., Johnson, J. A., Plez, B., et al. 2010, A&A, 509, A93
Masseron, T., Merle, T., & Hawkins, K. 2016, BACCHUS: Brussels Automatic Code for Characterizing High accUracy Spectra, Astrophysics Source Code Library, ascl:10.20356/C4TG6R
Mészáros, S., Martell, S. L., Shetrone, M., et al. 2015, AJ, 149, 153
Milone, A. P., Marino, A. F., Piotto, G., et al. 2015, ApJ, 808, 51
Monari, G., Famaey, B., Siebert, A., et al. 2017a, MNRAS, 465, 1443
Monari, G., Kawata, D., Hunt, J. A. S., & Famaey, B. 2017b, MNRAS, 466, L113
Mura-Guzmán, A., Villanova, S., Muñoz, C., & Tang, B. 2018, MNRAS, 474, 4541
Myeong, G. C., Vasiliev, E., Iorio, G., Evans, N. W., & Belokurov, V. 2019, MNRAS, 488, 1235
Ostdiek, B., Necib, L., Cohen, T., et al. 2019, arXiv:1907.06652
Pinsonneault, M. H., Elsworth, Y. P., Tayar, J., et al. 2018, ApJS, 239, 32
Piotto, G., Milone, A. P., Bedin, L. R., et al. 2015, AJ, 149, 91
Portail, M., Gerhard, O., Wegg, C., & Ness, M. 2017, MNRAS, 465, 1621
Queiroz, A. B. A., Anders, F., Santiago, B. X., et al. 2018, MNRAS, 476, 2556
Ramírez, I., Meléndez, J., & Chanamé, J. 2012, ApJ, 757, 164
Randich, S., Gilmore, G. & *Gaia*-ESO Consortium 2013, Msngr, 154, 47
Robin, A. C., Marshall, D. J., Schultheis, M., & Reylé, C. 2012, A&A, 538, A106
Robin, A. C., Reylé, C., Derrière, S., & Picaud, S. 2003, A&A, 409, 523
Robin, A. C., Reylé, C., Fliri, J., et al. 2014, A&A, 569, A13
Savino, A., & Posti, L. 2019, A&A, 624, L9
Schiappacasse-Ulloa, J., Tang, B., Fernández-Trincado, J. G., et al. 2018, AJ, 156, 94
Schiavon, R. P., Zamora, O., Carrera, R., et al. 2017, MNRAS, 465, 501
Schönrich, R., & Aumer, M. 2017, MNRAS, 472, 3979

Simpson, J. D., & Martell, S. L. 2019, MNRAS, 490, 741
Tang, B., Cohen, R. E., Geisler, D., et al. 2017, MNRAS, 465, 19
Tang, B., Fernández-Trincado, J. G., Geisler, D., et al. 2018, ApJ, 855, 38
Tang, B., Liu, C., Fernández-Trincado, J. G., et al. 2019, ApJ, 871, 58
Vasiliev, E. 2019, MNRAS, 484, 2832
Ventura, P., Di Criscienzo, M., Carini, R., & D'Antona, F. 2013, MNRAS, 431, 3642
Vesperini, E., & Heggie, D. C. 1997, MNRAS, 289, 898
Villanova, S., Geisler, D., & Piotto, G. 2010, ApJL, 722, L18
Weinberg, M. D. 1994, AJ, 108, 1414
Wu, Y., Luo, A.-L., Li, H.-N., et al. 2011, RAA, 11, 924
Yan, H.-L., Shi, J.-R., Zhou, Y.-T., et al. 2018, NatAs, 2, 790
Yong, D., Grundahl, F., & Norris, J. E. 2015, MNRAS, 446, 3319
Zhang, B., Liu, C., & Deng, L.-C. 2020, ApJS, 246, 9
Zhao, G., Zhao, Y.-H., Chu, Y.-Q., Jing, Y.-P., & Deng, L.-C. 2012, RAA, 12, 723